Role of Coherent Structures on Reynolds Stresses in a 2-D Bubble Column

R. F. Mudde, D. J. Lee, J. Reese, and L.-S. Fan
Dept. of Chemical Engineering, The Ohio State University, Columbus, OH 43210

The hydrodynamics of two-dimensional bubble columns operated in various flow regimes are studied using particle image velocimetry. Both averaged velocity profiles and Reynolds stress profiles are obtained and discussed in relation to large-scale structures present in the flow. The normal stresses, dominated by large-scale structures, are an order of magnitude higher than the shear stress. It is found that the contribution from the bubbles to the shear to the normal stresses is negligible. A time series of the flow field is studied, demonstrating that the flow could be split into a low-frequency contribution due to the vortical structures and a high-frequency fluctuating part. The latter gives rise to flat normal stress profiles, and the former is responsible for the original form of the normal stress profiles. The shear stress in the smaller columns investigated can be related to the averaged vertical velocity profile according to a Boussinesq approximation. Data on the eddy viscosity are presented.

Introduction

In the study of bubble column systems, it has become apparent that the quantification of the instantaneous, rather than the time- or volume-averaged, hydrodynamic flow phenomena is required to provide further insight to the design and scale-up of such systems (Tzeng et al., 1993; Yang et al., 1993; Chen et al., 1994; Lapin and Lübbert, 1994; Devanathan et al., 1995; Grevskott et al., 1996; Groen et al., 1996). Data on the instantaneous flow behavior of bubble columns, however, are scarce in the literature. This is because of the difficulties encountered in performing the necessary measurements. Few experimental techniques are available to probe the details of the flow field, for example, tracking of a radioactive particle (Devanathan et al., 1990; Yang et al., 1993), hot-wire anemometry (Franz et al., 1984; Menzel et al., 1990), and laser Doppler anemometry (Franz et al., 1984; Groen et al., 1996). These techniques essentially provide point information. The ability to quantify the instantaneous flow *field* of bubble columns has only recently been realized through the use of a particle image velocimetry (PIV) system as developed by Chen and Fan (1992). The PIV system is a noninstrusive technique that allows for the measurement of the full-field flow information; thus, the PIV system has the capability of assessing the coupling effects of the flow field that may be lost when using point measurement techniques. The PIV system, furthermore, allows for the simultaneous measurement of each phase; thus, the liquid velocity and gas distribution can be determined at any instant for a given plane in a bubble column.

The characterization of the instantaneous hydrodynamic properties of bubble columns is a challenging issue. Tzeng et al. (1993) characterized the instantaneous flow phenomena of a 2-D bubble column through the use of flow visualization, while Chen et al. (1994) studied the instantaneous flow phenomena of a three-dimensional (3-D) bubble column using flow visualization and a PIV system. In both cases the instantaneous macroscopic flow phenomena were delineated; furthermore, through the use of the PIV system, Chen et al. (1994) demonstrated that the instantaneous macroscopic phenomena were lost when the flow information was averaged. In order to provide further insight to the instantaneous behavior of bubble columns, however, a more complete analysis of smaller scales or microscopic phenomena is required. These microscopic phenomena can be associated with the gas phase, such as bubble coalescence and breakup, or with the liquid phase in the form of fluctuating velocities, turbulence intensities, and Reynolds stress terms.

Franz et al. (1984) used a hot-film anemometer technique to measure the axial, radial, and tangential liquid velocities and identified the importance of the dynamic nature of the

---

Correspondence concerning this article should be addressed to L.-S. Fan.

Permanent address of R. F. Mudde: Kramers Laboratorium voor Fysische Technologie, Delft University of Technology, Delft, The Netherlands.

flow structure in a 3-D bubble column system. The liquid velocity and turbulent intensity profiles were obtained by averaging the point measurements at several different axial and radial locations. They found that the axial turbulence intensity was significantly higher than those in the radial and tangential directions and that the axial turbulence intensity varied in the radial direction, while the radial and tangential turbulence intensities were rather uniform. The region of largest axial turbulence intensity was identified to be between the central upward bubble flow and downward flow near the column wall.

Menzel et al. (1990) measured the point axial and radial liquid velocities simultaneously using a hot-film anemometry with triple split probes. The technique has the capability of measuring the axial and radial turbulence intensities as well as the Reynolds shear stress. They found that the radial profile of the Reynolds shear stress had a familiar shape and corresponded well with the radial profile of the axial liquid velocity. The shear stress was determined to have its greatest absolute value in the region where the axial velocity gradient was highest and to have a value of zero where the averaged axial velocity was maximum, that is, the column center, thereby suggesting a Boussinesq type of correlation between the averaged axial velocity and the shear stress. Profiles similar to Franz et al. (1984) were determined for the axial and radial turbulence intensities. Yang et al. (1993), using a computer-automated radioactive particle tracking (CARPT) technique, also measured the Reynolds stresses in a bubble column system. By tracking a single radioactive particle over a long period of time, they determined the radial profiles of the Reynolds shear stress, and the axial and radial normal stresses. They found similar profiles for the Reynolds shear stress. However, they mentioned that with the CARPT facility it was difficult to measure the Reynolds shear stress near the column center and close to the column wall. Interestingly, though, they reported that the axial and normal stresses were considerably greater than the Reynolds shear stress. Therefore, they concluded that ignoring the normal turbulent stresses in any modeling attempts needed to be reconsidered.

This study demonstrates for the first time the full-field measurement of Reynolds shear and normal stresses in 2-D bubble columns through the use of a PIV system. Two-dimensional bubble columns can be used because, as just described, the tangential velocity component is much less than the axial and radial components, especially at low gas velocity. Even though there are limitations in similarity between 2- and 3-D bubble columns, the structures present in the flow field in 2-D cases can qualitatively enlighten a better understanding of those in 3-D cases (Reese et al., 1993). The use of the PIV system allows for a more complete analysis of the quantitative flow information that is much needed in the development and verification of modeling studies.

Experimental Setup

The experimental apparatus is shown in Figure 1. The 2-D bubble column is made of Plexiglas and the viewing section of the column is 48.2 cm in width, 160 cm in height, and 1.27 cm in depth. Two movable vertical partitions in the viewing section allow the width of the bed to be varied from 11.2 cm to the full width of 48.2 cm when the partitions are removed. Below the viewing section is the liquid distributor, which consists of a packed particle section and a liquid calming section. The gas distributor is made up of nine tube injectors flush mounted on the column wall at the bottom of the viewing section. Each gas injector opening is 1.6 mm ID, creating an initial bubble size of about 5 mm. The gas flow through each injector is individually regulated by a needle valve connected to the plenum compartment outside of the bed. The distance between two adjacent bubble injectors is 51 mm, and that between the end injector and the sidewall is 37 mm. When the width of the column is changed, the number of gas injectors required also changes. There is no liquid or gas flow through the region beyond the partition.

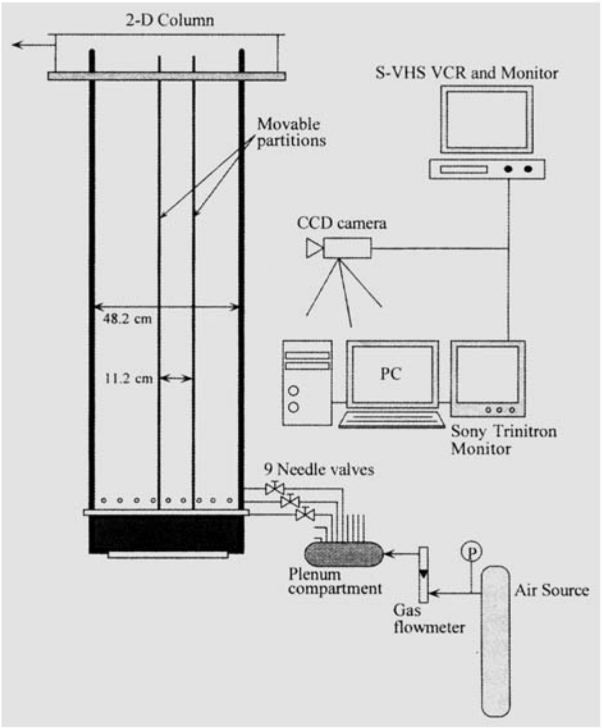

Figure 1. Experimental apparatus.

Tap water is used as the liquid phase. The liquid phase is operated under batch conditions and the static liquid height is kept constant at 110 cm for all tests in this study. Neutrally buoyant Pliolite particles with a size range of 500–600 μm are used as the liquid tracer. Air is used as the gas phase. The gas pressure is maintained within 128–170 kPa upstream of the gas plenum. The superficial gas velocity ranges from 0.4 to 1.9 cm/s at 25°C and 1 atm in this study. All the gas velocities described in the text refer to superficial velocities at 25°C and 1 atm unless otherwise stated. Table 1 lists the column width and superficial gas velocities used; the overall gas holdup; the height, h, at the center of the field of view above the gas inlets where the PIV measurements are conducted; and the height, H, and the width, W, of the field of view. Notice that for the 32-cm column the left side is always investigated, while the righthand side is checked for (a)symmetry of the flow field. Note that the left and right sides are marked by L and R; the fields of view are denoted as bottom, lower, middle, and upper section for $h = 9$, 30, 55, and 75 cm, respectively.

Table 1. Experimental Conditions

Column Width (cm)	U_{sup} (cm/s)	Holdup %	h (cm)				$H \times W$ (cm^2)
11.2	1.0	1.3			55	75	11×11.2
15.2	1.0	1.5		30	55	75	12×15.2
	1.3	2.0		30	55	75	12×15.2
32	0.4	1.1		30 (L)	55 (L+R)		15×18
	0.6	1.5		30 (L)	55 (L)		15×18
	1.2	2.8	9 (L)	30 (L)	55(L+R)	75 (L)	15×18
	1.9	4.2			55 (L)		15×18

Particle Image Velocimetry Technique

The PIV system developed by Chen and Fan (1992) is applied to measure the instantaneous full-field flow information of the 2-D bubble column. A high-resolution (800 × 490 pixels) charge-coupled device (CCD) camera equipped with variable electronic shutter ranging from 1/60 to 1/8,000 s is used to record the image of the flow field. The flow field is illuminated by properly placed incandescent light. The recorded images are stored on videotapes in a S-VHS VCR and later analyzed by a PC (Pentium 120 MHz or 486/50 MHz IBM/DX). A Data Translation DT 2861, a 512-×418-×8-bit frame-grabber board with a maximum of 16 frames using 256 gray levels per frame, is used to digitize the images. The frame-grabbing speed is 1/30 s, while each frame consists of two interlaced video fields with a time interval of 1/60 s.

The PIV technique used here operates at low seeding densities (typically a few particles per cm^2 viewed), and utilizes a particle-tracking algorithm to determine the velocity fields. This mode of PIV operation is commonly referred to as particle-tracking velocimetry (PTV). The technique discriminates between seeding particles and bubbles based on the size of the recorded image of the objects. In this article no analysis of the bubble phase is presented since the focus is on the liquid flow. The image processing occurs in five steps: (1) image acquisition, (2) image enhancement, (3) particle identification and calculation of the centroids, (4) discrimination of the particle images between the two phases, and (5) matching of the particles in three consecutive video fields and calculation of the velocity of the identified triplets. A full description of the PIV system and technique can be found in Chen and Fan (1992) and Reese et al. (1995).

Definition of averaged quantities

The vectors obtained are located at the position of the centroid of the initial tracer particle in a triplet. Profiles are calculated by dividing the field of view into vertical strips that have a specified width and cover the entire height of the field of view. A given vector $\{u(x,y),\ v(x,y)\}$ is attributed to a particular strip when the centroid of the initial tracer particle of a triplet is located in that strip; u and v are the horizontal and vertical component of the velocity; and x and y are the horizontal and vertical coordinates, respectively, with the origin located at the bottom center of the column in-line with the gas injectors. The average of the velocity components and the various Reynolds stresses for all fields for each strip are then calculated as specified in Eqs. 1 to 5 as given in Table 2.

A disadvantage of this method may be that all vectors are weighed equally; hence, a cluster of vectors at a certain location in a particular frame, with all vectors approximately the same, will have a large influence on the averages in that particular strip. However, it does not necessarily give more information about the flow than an isolated vector. The spatial distribution of vectors is an immediate consequence of the seeding distribution, and may have little to do with the flow field. Another averaging procedure is tested in which, for a given vector field, the vectors in grid cells are first averaged to obtain the velocity at that moment in the cell. Note that a 15-by-10 grid is used with data from the 15-cm column. The averaged quantities of the flow are then calculated by averaging all cell-averaged fields of the various vector fields. The difference between the two methods is small, so all averaged quantities presented below are calculated according to the first method.

Influence of seeding on turbulence, response time

The seeding of Pliolite particles of size ≈ 0.5 mm and density ≈ 1,020 kg/m^3 yields a Stokes response time of about 1.4 $\times 10^{-2}$ s, or alternatively a frequency of 70 Hz. This is slightly higher than the frequency at which the fields are

Table 2. Equations for Obtaining the Averaged Velocities and Stresses

Averaged horizontal velocity	$\langle u(i)\rangle = \frac{1}{N(i)} \sum_{\{x,y\}\in \mathrm{strip}(i)} u(x,y)$	(1)
Averaged vertical velocity	$\langle v(i)\rangle = \frac{1}{N(i)} \sum_{\{x,y\}\in \mathrm{strip}(i)} v(x,y)$	(2)
Horizontal normal stress	$\langle u'u'\rangle(i) = \left[\frac{1}{N(i)} \sum_{\{x,y\}\in \mathrm{strip}(i)} u(x,y)u(x,y)\right] - (\langle u(i)\rangle)^2$	(3)
Vertical normal stress	$\langle v'v'\rangle(i) = \left[\frac{1}{N(i)} \sum_{\{x,y\}\in \mathrm{strip}(i)} v(x,y)v(x,y)\right] - (\langle v(i)\rangle)^2$	(4)
Shear stress	$\langle u'v'\rangle(i) = \frac{1}{N(i)} \sum_{\{x,y\}\in \mathrm{strip}(i)} [\{u(x,y)-\langle u(i)\rangle\}\{v(x,y)-\langle v(i)\rangle\}]$	(5)

with $N(i)$ the number of vectors in strip i (usually between 1,000 and 1,500).

processed. Smaller particles would be desirable, but with the large field of view, small particles would result in poor images. According to Elghobashi (1994) the influence of the particles on the turbulence in particle-laden flows is a function of the volumetric particle density and the ratio of the particle response time, τ_p, to the time scales of the turbulence, that is, the Kolmogorov time scale, τ_K, and the turnover time of the large eddies, τ_e. The Kolmogorov time scale τ_K is estimated from $(\nu/\epsilon)^{1/2}$, where ν is the kinematic viscosity of water and ϵ is the energy dissipation per unit volume. The energy dissipation ϵ is close to gU_{sup} where g is the acceleration of gravity and U_{sup} is the superficial gas velocity. These substitutions for ν and ϵ result in $\tau_K = 3.2 \times 10^{-3}$ s. The turnover time is estimated from $\tau_e = l/u_e$, where l is the characteristic length scale of the energy containing eddies and u_e is the rms fluid velocity. The characteristic length scale l is taken to be the average size of the large-scale vortical structures, which in this case is approximately 10 cm for the 15-cm column (Lin et al., 1996), while the rms fluid velocity u_e is obtained from the present investigation, and the experimental value of 20 cm/s is used. The substitutions of l and u_e give $\tau_e = 0.5$ s. The volume fraction of particles is on the order of 10^{-6} to 10^{-5}. Extrapolating Elghobashi's rules for particle-laden turbulent flows shows that the seeding in the present study is at the border of "negligible influence on turbulence" and "particles enhance dissipation," furthermore, the preceding estimates show that (1) the particle response time is slightly lower than the time between consecutive video fields; (2) the particle response time is much smaller than the time scale of the energy containing eddies; and (3) the smallest scales cannot be resolved with the present particles.

Two-Fluid Model and Reynolds Stress

The dispersed two-phase flow in a bubble column can be described in an Eulerian way by the two-fluid model. This model describes the averaged motion for each of the two phases. The general form of the governing equations is well established. The averaged momentum equation for the liquid phase, for instance, can be given by

$$(1-\alpha)\rho_l\left(\frac{\partial}{\partial t} + v_l \cdot \nabla\right)v_l = -(1-\alpha)\nabla p - (1-\alpha)\nabla \cdot \boldsymbol{\tau} - \nabla \cdot (1-\alpha)\rho_l \langle v_l' v_l' \rangle + (1-\alpha)\rho_l g + F_s, \quad (6)$$

where α is the void fraction, ρ_l is the liquid density, v_l is the averaged liquid velocity, p is the pressure, $\boldsymbol{\tau}$ is molecular shear stress, and F_s is the interaction force density with the gas phase. The third term on the righthand side is a consequence of the averaging of the local and instantaneous momentum equation of the liquid, and is referred to as the Reynolds stress, τ_{Re}, where v_l' is the fluctuating part of the local and instantaneous velocity, and the bracket denotes averaging. This term is comparable to the Reynolds stresses encountered in describing single-phase turbulent flows; however, it should be noted that the Reynolds stresses are due to not only "turbulent fluctuations" in the liquid phase but also to the motion of the dispersed particles.

The equation of motion has various terms that need to be modeled, the well-known closure problem. Added mass effects, lift forces, drag, and other fluid force terms are incorporated in the mutual interaction force. The Reynolds stresses require a separate closure. Both shear-induced and bubble-induced "turbulence" will have to be considered. Unfortunately, little is known of the coupling between these two, especially in the case of buoyancy-driven air/liquid flows found in bubble columns. Lopez de Bertodano et al. (1994) assumed for low holdup bubbly flow in pipes that the shear- and bubble-induced turbulence are only weakly coupled so that the Reynolds stress is a linear combination of the two effects:

$$\tau_{Re} = \tau_{Re}^{BI} + \tau_{Re}^{SI}. \quad (7)$$

The bubble-induced contribution is calculated using potential flow theory around a single bubble (Nigmatulin, 1979). The general form is

$$\tau_{Re}^{BI} = 2\begin{pmatrix} 4/10 & 0 & 0 \\ 0 & 3/10 & 0 \\ 0 & 0 & 3/10 \end{pmatrix} k^{BI}, \quad (8)$$

where k^{BI} is the kinetic energy density associated with the flow field around the bubble. This energy is calculated from the potential theory:

$$k^{BI} = \frac{1}{2}\alpha \rho_l C_{vm} v_s^2, \quad (9)$$

where v_s is the slip velocity between the bubbles and the liquid, and C_{vm} is the virtual mass coefficient, which has an approximate value of 2 for bubbles with a diameter of 5 mm (Lance and Bataille, 1991). In a later section it will be seen that in the present case this contribution to the normal stresses can be neglected.

The shear-induced part of the Reynolds stress can be modeled with various degrees of complexity. One of the most simple approahces employs the concept of eddy viscosity:

$$\tau_{Re}^{SI} = -\rho_l \nu_t (\nabla \vec{v}_l + \nabla \vec{v}_l^T), \quad (10)$$

where the eddy viscosity ν_t can be further modeled using the k-ϵ model:

$$\nu_t = C_\mu \frac{k^2}{\epsilon}. \quad (11)$$

The constant C_μ is usually taken to be 0.09, and k and ϵ denote the turbulent kinetic energy density and the dissipation rate of turbulent kinetic energy, respectively. Notice that no extra terms attributed to the presence of the bubbles are included.

Sato et al. (1981) modeled the Reynolds shear stress differently. They split the velocity field into its average, $\langle v \rangle$, and two fluctuating contributions, v' and v''. The first fluctuating contribution v' represents the turbulence in the liquid phase independent of the bubbles, that is, the shear induced stress mentioned earlier, whereas the latter, v'', is caused by the agitation of the bubbles directly. Assuming the two to be uncorrelated, Sato et al. (1981) expressed the Reynolds shear stress as

$$\tau_{Re} = -\rho_l\langle u'v'\rangle - \rho_l\langle u''v''\rangle. \tag{12}$$

For both contributions, the eddy viscosity concept is introduced, thereby assuming that the bubble-induced stress is proportional to the gradient of the mean liquid flow. As a result,

$$\tau_{Re} = -\rho_l\nu_t'\frac{d\langle v\rangle}{dx} - \rho_l\nu_t''\frac{d\langle v\rangle}{dx}. \tag{13}$$

Although the last assumption may be questionable, the outcome is useful for a quick estimation of both contributions to the stress. The eddy viscosity of the bubble-dependent part is taken as proportional to the void fraction, the bubble radius R, and the slip velocity v_s. The result is

$$\tau_{Re} = -\rho_l(\nu_t' + k_1\alpha R v_s)\frac{d\langle v\rangle}{dx}. \tag{14}$$

The coefficient k_1 is an empirical constant with a value of 1.2 (Sato et al., 1981). Using the same values as indicated in the previous section, that is, 15-cm column at $U_{\text{sup}} = 1$ cm/s and average void fraction $\approx 1.5\%$, and modeling ν_t' with a k-ϵ model give for the shear-induced turbulent viscosity a value of 4×10^{-4} m²/s, whereas the bubble-induced viscosity is only about 2×10^{-5} m²/s. This result indicates that the contribution to the "turbulence" from the flow around the individual bubbles is negligible.

Description of the Flow Field

Two different flow regimes are of importance in the present study. For low gas flow rates the flow is in the dispersed regime with little or no bubble–bubble interaction. At higher gas flow rates, that is, $U_{\text{sup}} \geq 1$ cm/s in the 2-D column, the coalesced regime is encountered. For the 2-D column the coalesced regime can be split into a four-region flow condition observable in columns with a width greater than 20 cm at moderate gas rates (Tzeng et al., 1993; Lin et al., 1996) and a three-region flow condition. The three- and four-region flows are characterized by an averaged gross scale circulation of the liquid, with liquid rising in the center and descending near the wall. In the descending flow regions, vortical structures are observable that travel downward. Adjacent to this vortical flow region is the fast bubble region. The bubbles injected at the bottom cluster together to move upward in a wavylike manner, forming this fast bubble region. The difference between the three- and four-region flow conditions is that in the four-region flow two fast bubble flow regions are formed at each side of the column and are separated by a central plume region. The coalescence is much less in the central plume region, and the bubble–bubble interactions are less important. In the three-region flow condition the two fast flow regions merge, with the central plume region disappearing. The flow structure in the three-region flow condition is shown in Figure 2; furthermore, several representative examples of the liquid velocity fields obtained through the PIV technique in the 11-cm column are shown in Figure 3. The swinging motion of the fast bubble stream and the vortical structures are evident in the figures. Tzeng et al. (1993) and Lin et al. (1996) provide detailed qualitative de-

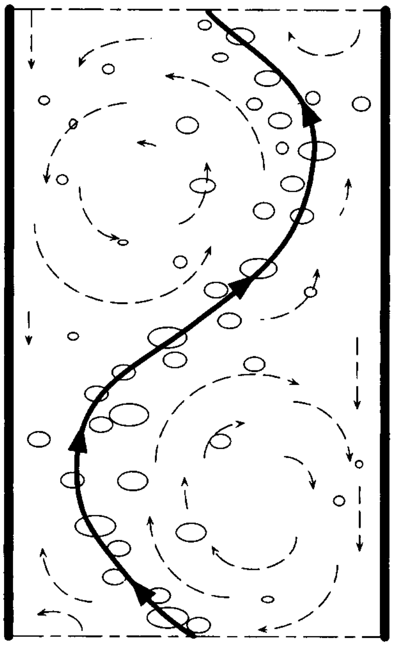

Figure 2. Flow structure for the three-region flow.

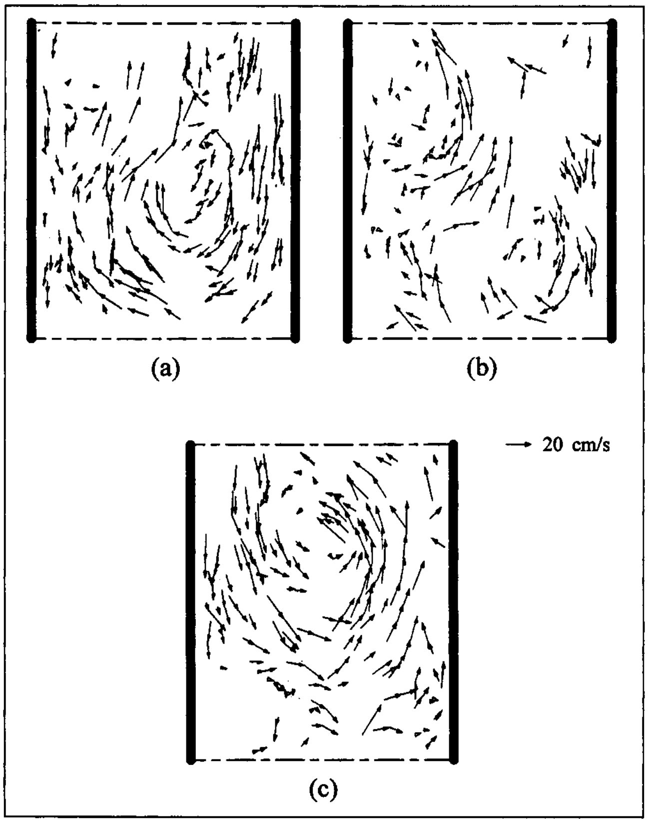

(a) (b)

(c)

Figure 3. Sample PIV results of the flow field in the middle section of the 11-cm column at a superficial gas velocity of 1 cm/s.

scriptions of the flow regimes and quantitative assessments of the macroscopic flow structures in various-size 2-D columns.

The flow field in a 3-D cylindrical bubble column can be classified in a similar manner. At low gas velocities the bubble flow is classified as the dispersed regime, while at higher superficial gas velocities the coalesced regime is observed. The bubbles cluster and coalesce at higher gas flow rates, forming a central bubble stream that moves in a wavy-spiral motion throughout the column. The liquid is carried upward in this bubble stream and flows downward in the region between bubble stream and the column wall. In this descending region, vortical structures are found that behave quite like those in the 2-D columns (Chen et al., 1994). The similarity between the flow behavior in 2- and 3-D columns is the reason for investigating the flow in 2-D columns in great detail.

Results of the 11-cm and 15-cm Cases

Averaged velocity profiles

The averaged profiles of the velocity and stresses are obtained by analyzing at least 80, or in most cases 120, randomly grabbed pairs of frames that yield vector fields such as those shown in Figure 3. Note that all the pairs of frames are acquired within 10 to 15 minutes of video recording. For such a set of vector fields, the averaged velocities are computed in vertical strips with a height equal to the field of view and a horizontal width of about one centimeter. The averaged profiles obtained are verified to ensure that the profiles do not change significantly when increasing the number of independent fields above 80. This is particularly true for the vertical component of the velocity. Figures 4 and 5 demonstrate typical examples for the averaged profiles obtained in the small columns.

The familiar gross scale circulation previously reported by numerous researchers (e.g., Hills, 1974; Franz et al., 1984; Menzel et al., 1990) is evident from Figures 4 and 5. The maximum upward as well as the maximum downward velocity is about 10 cm/s in both cases. It should be noted that the profiles are the result of averaging the swinging motion of the central bubble stream and the related structures present, instantaneously in the flow. In these cases, the averaged gas holdup profile also shows the familiar shape, that is, a maximum in the center and decreasing to zero toward the wall. Figure 5 demonstrates that the averaged flows in the middle and upper sections are similar; however, they differ somewhat from the one in the lower part of the column. This is the general trend in the 11-cm and 15-cm cases, that in the lower section of the column the flow is not developed. Notice that, especially in the 11-cm case as given in Figure 4, the averaged horizontal component of the velocity $\langle u \rangle$ is not zero, but that an inward flow is observed. This is the general trend, even in the upper sections of the column. Similar phenomena have been reported by Menzel et al. (1990) in a 3-D column. A reason for this nonzero averaged horizontal velocity is the difficulty in tracking the particles in the fast-moving bubble stream. In addition to the high velocities encountered in the bubble stream that make the matching of the triplets more difficult, the tracers are also frequently secluded either behind or in front of a cluster of bubbles. Note that the local holdup is much higher in the bubble stream than elsewhere; hence, an underprediction of the high velocities can be expected. Calculation of the net vertical liquid flow reveals that indeed a net downward flow is measured. In the bubble stream the vertical velocity of the liquid tracers is always positive. It is clear that if the stream crosses the field of view from lower right to upper left, the liquid descending in the right wall region is drawn into the bubble stream at high velocities, as seen in Figure 3a. The high velocities in this descending/vortical region, directed toward the middle of the column, are easily obtained with the PIV. This visual inspection explains a systematic error, that is, not enough vectors with high positive vertical velocity components and high hori-

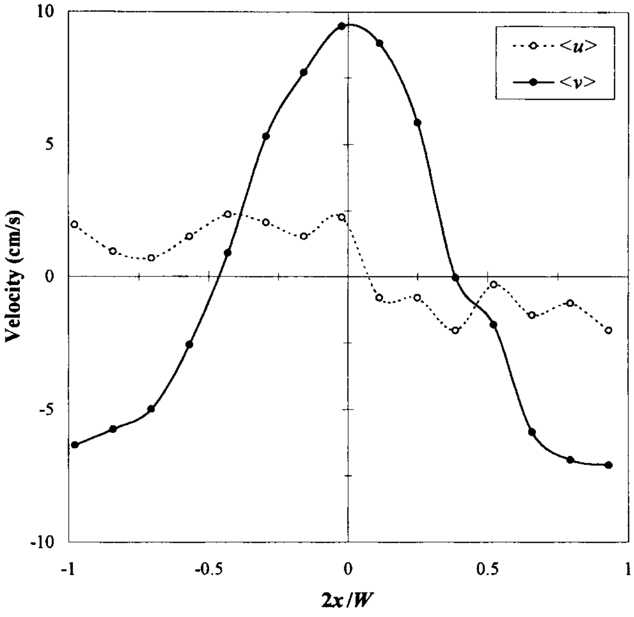

Figure 4. Averaged velocity profiles for the middle section of the 11-cm column at $U_{sup} = 1.0$ cm/s.

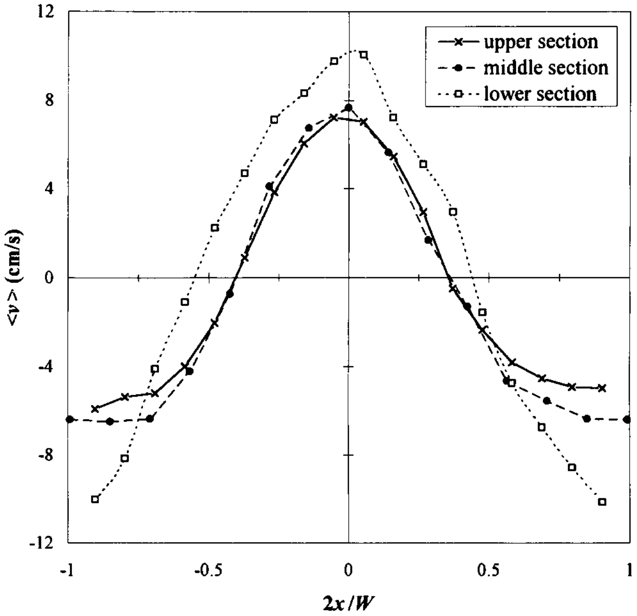

Figure 5. Averaged velocity profiles for the 15-cm column at $U_{sup} = 1.0$ cm/s.

zontal velocity vectors toward the wall are found; however, this systematic error is not observable in Figure 3c. In order to arrive at zero mean horizontal velocity, an extra 5% to 10% of these "lost" vectors are necessary. The addition of the "lost" vectors, however, leads to an overall mass balance that shows a net upward liquid flow.

Probability density function of the velocity

As mentioned earlier, the flow is characterized by the appearance of vortical structures that move downward adjacent to the wall regions. The alternating vortices dominate the form of the probability density functions (*pdf*'s) of the vertical component of the liquid velocity. For instance, in the 11-cm case as shown in Figure 6, for a strip in the wall region the contribution of the vortices to the *pdf* causes a high negative peak, whereas the vortex that flows downward at the opposite side gives a smaller local maximum at positive velocity in the *pdf*. Moving toward the center of the column, the significance of the positive peak increases and the negative peak decreases so that a "shoulder" is formed in the *pdf*. In the center the negative peak is hidden in the bell-shaped curve; however, negative velocities are still observed showing the dynamic nature of the flow. In a recent article, Groen et al. (1996) reported measurements of the vertical component of the liquid velocity in 3-D bubble columns of 15- and 23-cm ID using laser Doppler anemometry. They obtained similar *pdf*'s and concluded that the vortical structures can be measured in their 3-D columns. These results indicate that many of the findings reported in the present study of 2-D columns also reflect the hydrodynamics in the 3-D column.

Reynolds stresses

The Reynolds normal and shear stresses are calculated directly from the vector fields using Eqs. 3, 4, and 5 in Table 2.

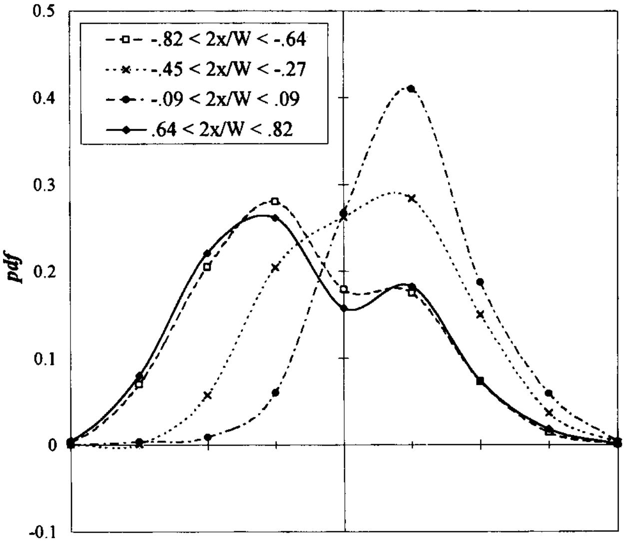

Figure 6. Probability density functions of the vertical velocity component for the 11-cm column at $U_{sup} = 1.0$ cm/s.

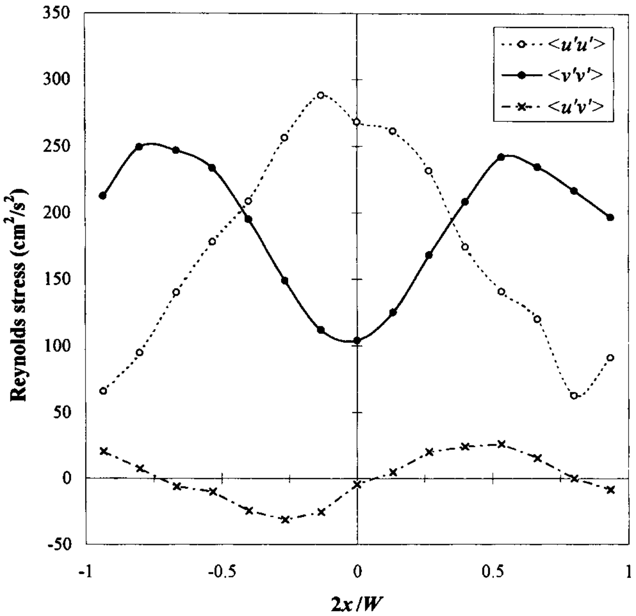

Figure 7. Profiles of the Reynolds stresses component for the middle section of the 15-cm column at $U_{sup} = 1.0$ cm/s.

An example is shown in Figure 7 for the middle section of the 15-cm column at $U_{sup} = 1$ cm/s using 177 independent vector fields. The stresses are clearly (anti-)symmetric around the column axis. The Reynolds normal stresses, $\langle u'u' \rangle$ and $\langle v'v' \rangle$, are an order of magnitude higher than the shear stress $\langle u'v' \rangle$. This is in agreement with the findings of Yang et al. (1993). In the 11-cm and 15-cm columns, the profiles of the normal stresses are similar to those of Figure 7 in all cases investigated, that is, $\langle u'u' \rangle$ peaks in the center, whereas $\langle v'v' \rangle$ peaks close to the wall. The nature of the normal stresses is evident by considering the swinging motion of the central bubble stream. In the center of the column, the flow is more frequently upward, whereas closer to the wall, in the region defined as the vortical flow region by Lin et al. (1996), the flow dynamically changes from upward to downward, depending on the location of the central bubble stream. The flow in this region therefore experiences large fluctuations in the vertical component of the liquid velocity, leading $\langle v'v' \rangle$ to peak closer to the wall than in the center where the motion is primarily directed upward. The swinging motion of the central bubble stream leads to the peaking in $\langle u'u' \rangle$ at the central portion of the column, since the horizontal velocity attains its highest magnitude in the center, while the rather uniform downflow or upflow closer to the wall regions does not contribute as significantly to the radial fluctuations. Alternatively, the nature of the normal stresses can be explained by the dominance of the flow by the vortical structure and can be understood from the following illustration, as shown in Figure 8. When a vortical structure moves past a fixed point P located close to the wall, a large contribution to $\langle v'v' \rangle$ is measured since v' is large. However, the contribution to $\langle u'u' \rangle$ is small since u' is small. If the point P moves toward the center of the column, the contribution to $\langle u'u' \rangle$ becomes larger. At the center line the horizontal velocity of the vortex is at its maximum, hence $\langle u'u' \rangle$ peaks there. For

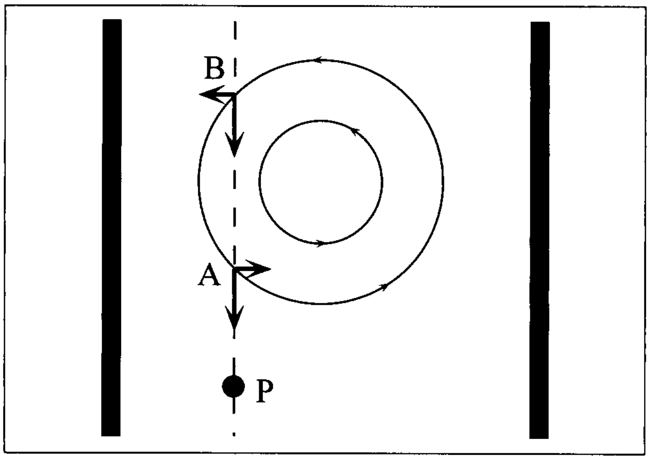

Figure 8. Vortical structure moving downward past point P.

$\langle v'v' \rangle$, the opposite is the case. The contribution to $\langle v'v' \rangle$ decreases toward the center since the contribution to v from the vortical structures vanishes because the vortices span the entire width of the column and v' decreases. Obviously, at the wall $\langle u'u' \rangle$ and $\langle v'v' \rangle$ drop to zero since both u and v become zero at the wall. For the shear stress $\langle u'v' \rangle$, the situation is different. Assuming that the vortices exhibit a circular motion, the contribution to $\langle u'v' \rangle$ at point A is exactly balanced by that at point B, that is, only u changes its sign. The contribution of another vortex with opposite circulation does not alter this picture. Both normal stresses are insensitive to the direction of the rotation. Turbulence intensities, defined as

$$I_u = \frac{\sqrt{\langle u'u' \rangle}}{\langle v \rangle_{\max}} \quad \text{and} \quad I_v = \frac{\sqrt{\langle v'v' \rangle}}{\langle v \rangle_{\max}} \tag{15}$$

are on the order of 200%. The characteristic values of the normal stresses in the 11-cm and 15-cm cases are summarized in Table 3.

The profile of the shear stress is, in general, more difficult to obtain from the vector fields than that of the normal stresses. One apparent reason is that contributions to $\langle u'v' \rangle$ can be both positive and negative, whereas those for the normal stresses are always positive. Furthermore, the difficulty with obtaining the vectors in the bubble stream, mentioned previously, also has a greater effect on $\langle u'v' \rangle$ than on the other stresses. In the left portion of the column negative contributions may be missed, that is, negative u and positive large v, and positive contributions may be missed in the right side. Comparison of the shear stress in Figure 7 and the averaged vertical velocity from Figure 7 illustrates that the shear stress and vertical velocity can be correlated via a Boussinesq approximation. The best fit of the data gives a value of 5.1×10^{-4} m^2/s for the eddy viscosity. A similar value can also be roughly estimated from a k-ϵ like calculation. As mentioned previously, in the standard k-ϵ model the eddy viscosity is calculated according to Eq. 11, with $C_\mu = 0.09$. If the turbulent kinetic energy per unit mass k is estimated as $\frac{1}{2}(\langle u'u' \rangle + \langle v'v' \rangle)$ (approximately equal to 180 cm^2/s^2) and the turbulent kinetic energy dissipation in the liquid is obtained from $\epsilon = g(U_{\text{sup}} - \langle \alpha \rangle v_s)$, a value of 4.9×10^{-4} m^2/s is obtained for the eddy viscosity ν_t. Note that the averaged holdup $\langle \alpha \rangle$ is 1.5% and the slip velocity v_s is approximately 25 cm/s. Similar data are calculated for the other cases. The results for the 11- and 15-cm columns are summarized in Table 4. Data on the eddy viscosity reported by Menzel et al. (1990) in a 3-D column with 60 cm ID are an order of magnitude higher.

Table 3. Characteristic Values of the Normal Stresses

Column Width (cm)	U_{sup} (cm/s)	h (cm)	$\langle u'u' \rangle_{\max}$ (cm^2/s^2)	$\langle v'v' \rangle_{\max}$ (cm^2/s^2)	$\langle v'v' \rangle_{\text{center}}$ (cm^2/s^2)
11.2	1.0	55	270	210	90
		75	300	280	100
15.2	1.0	30	170	190	75
		55	280	250	100
		75	230	200	75
	1.3	55	330	250	165

Table 4. Eddy Viscosities in the 11-cm and 15-cm Columns

Column Width (cm)	U_{sup} (cm/s)	h (cm)	ν_t(exp) (10^{-4} m^2/s)	ν_t(k-ϵ) (10^{-4} m^2/s)
11.2	1.0	55	5.4	4.0
		75	5.4	5.5
15.2	1.0	55	5.1	4.9
	1.3	55	5.0	6.4

Time series

For the middle section of the 15-cm case at $U_{\text{sup}} = 1$ cm/s, a series of 322 consecutive vector fields is constructed. The series comprises 10.73 s of the flow and contains the passage of two vortices in the field of view. Note that time between two vector fields or frames is 1/30 s. This analysis allows for the study of the flow dynamics in greater detail. For each field the liquid vectors are redistributed over a 10-by-10 grid. This is performed in the following way. All vectors in grid cell P in Figure 9 are averaged together with all vectors inside box Q but outside P, that is, the shaded area. The vectors in grid cell P are averaged with a weight factor of one, and the vectors in the shaded area are weighed with the inverse of the square of the distance from their location to the center of grid cell P. The resulting vector for each grid cell is assigned with coordinates (i, j):

$$v(i,j) = \frac{\sum\limits_{\{x,y\} \in Q} w(x,y) v(x,y)}{\sum\limits_{\{x,y\} \in Q} w(x,y)} \tag{16}$$

where $v(x,y)$ is the vertical component of the velocity of tracer particle with coordinates (x,y) and $w(x,y)$ is its corresponding weighing factor. A similar relation holds for the calculation of the horizontal component. Averaging over an area larger than a grid cell is necessary in order to avoid gaps in the time series of a grid cell caused by the inhomogeneous distribution of the vectors in the original fields. Obviously,

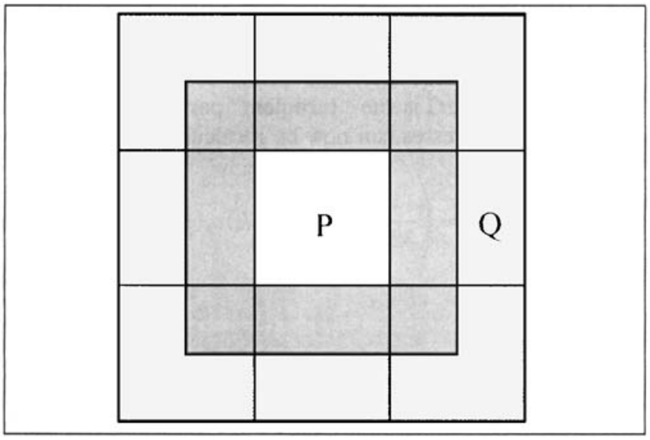

Figure 9. Grid and area used for averaging the velocity.

this operation renders a kind of "mesoscopic" picture of the flow field. The small-scale fluctuations and the noise are damped. The averaged velocity profiles for grid cells in any row are similar to those shown in Figure 5, although the profiles are not quite as symmetric because of a relatively small amount of data. After the cell average velocities are computed for the entire 10.73-s series, they are subtracted from the instantaneous vectors in the respective cells. In Figures 10a and 10b, the series of both components for grid cell (3,5) are shown. It should be noted that the left lower cell has coordinates (1,1). The vortical structures are clearly demonstrated, that is, periods of positive and negative axial velocity alternate. Plots for the other grid cells look similar with the exception of the cells adjacent to the walls, where the u-fluctuations are strongly damped, and the center cells, where the presence of the vortices is less dominant in the vertical velocity. Figure 11 shows the power spectral density functions

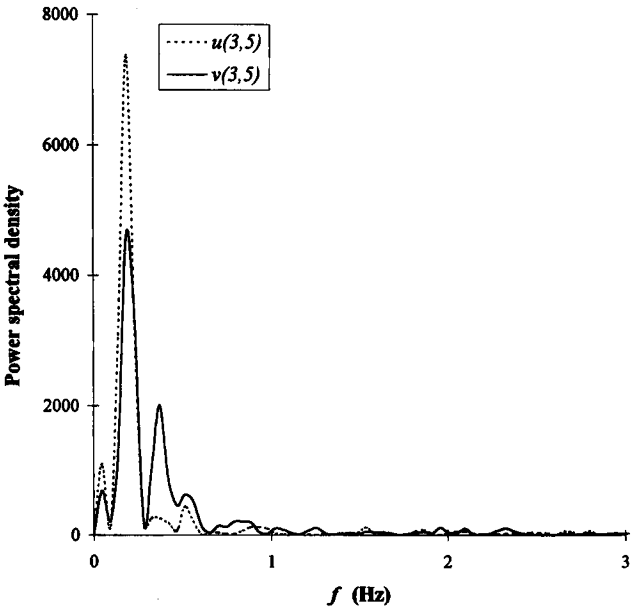

Figure 11. Power spectrum of the series shown in Figures 10a and 10b.

of both u and v for grid cell (3,5). Again, the vortical structures dominate, that is, hardly any power is found above 1 Hz, even up to the Nyquist frequency of 15 Hz. Cross-correlating of u-u for the cells on a horizontal row, that is, with the same j-coordinate, reveals that the u-components are in phase. The cross-correlation indicates that the vortices span the entire column width and flow as one big entity into the field of view. Similarly, cross-correlation of v-v for a row shows that the correlation of two cells on the same side of the column symmetry axis means zero-phase shift and on

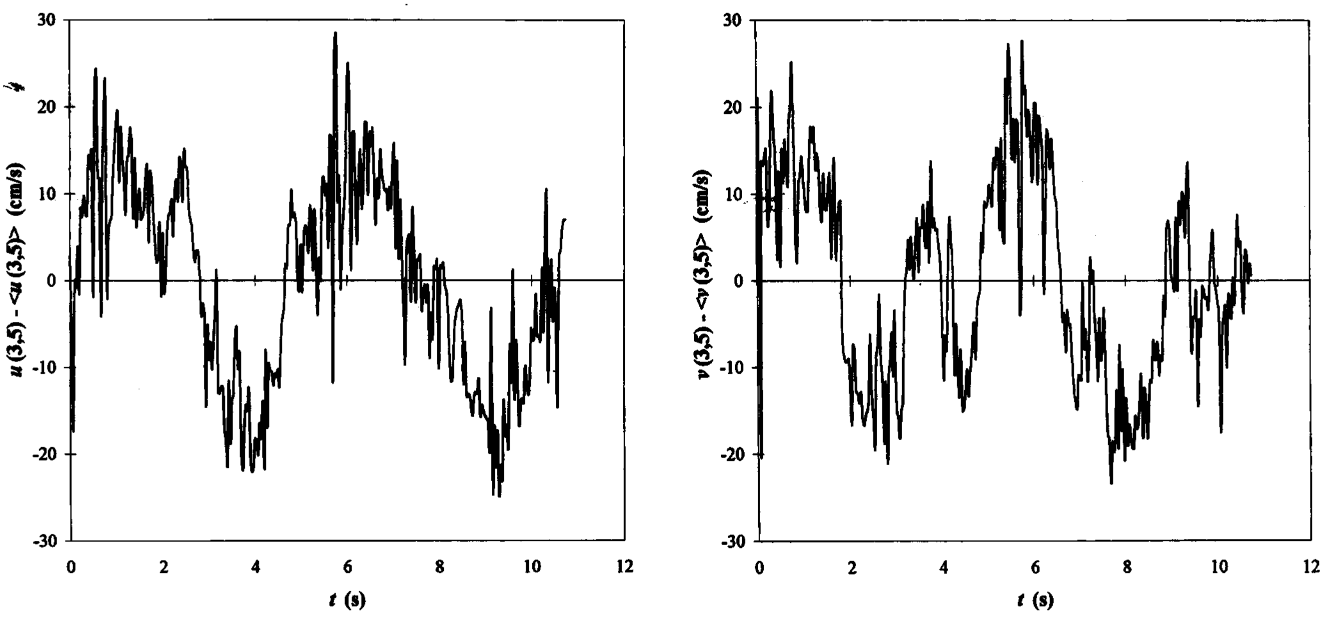

(a) (b)

Figure 10. Time series of the fluctuating component of: (a) horizontal velocity of cell (3,5); (b) vertical velocity of cell (3,5).

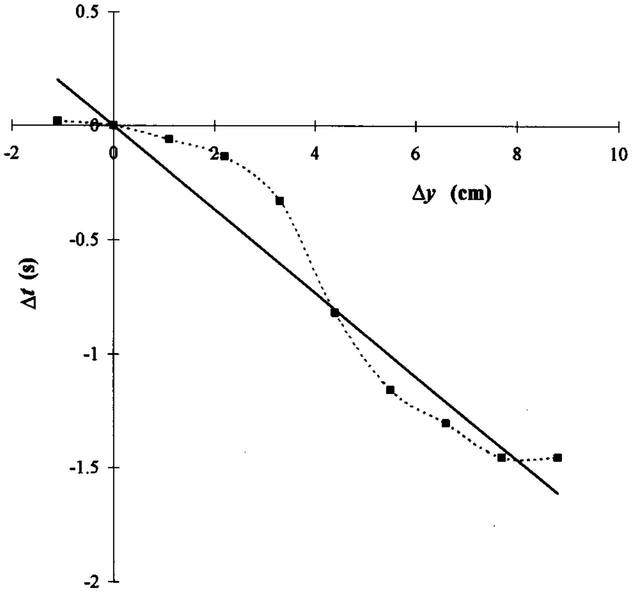

Figure 12. Time shift obtained from cross-correlating $v(2,2)$ and $v(2,j)$ as a function of the distance between the corresponding grid cells.

different sides gives a 180°-phase shift. In the latter case, different sides of the vortex are probed. Finally, from the cross-correlation between $v(2,2)$ and $v(2,j)$ with $j = 1$ to 10, a time shift, Δt, is found that increases with increasing distance, Δy, between the cells. In Figure 12 this time shift is plotted as a function of distance. Fitting a straight line through the data points gives a reasonable estimate of the descending velocity of the vertical structures. Note that the negative time shift means cell (2,2) responds later than cell $(2,j)$. The descending velocity of −5.5 cm/s is found, which is in agreement with the velocities reported by Lin et al. (1996) showing that the vortical structures are moving downward. This observation of the descending vortical structure differs from the results of Devanathan et al. (1995) who performed a 3-D simulation of the flow in a bubble column. Devanathan et al. reported that gas accumulating in the vortical structures leads to a decrease in the local density, thus causing the structures to rise. In the present case, the vortices are observed to entrap bubbles but still move downward. This behavior is probably due to the vortices being formed by a sudden increase in the magnitude of the downward flow in the wall region, which may imply that the overall momentum of the vortices is in the downward direction and inertia effects force them to move downward.

As previously mentioned, the large-scale vortical structures significantly influence the Reynolds normal stresses. The data from the time series demonstrate that the velocity field can be decomposed into a slow sinelike oscillation due to the passage of a vortex and high-frequency content associated with "turbulence" as shown in Figures 10a and 10b. The power spectra support the use of only one sinelike carrier wave for the vortices with a frequency around 0.2 Hz. As mentioned, the flow field can be decomposed according to

$$v(i,j;t) = \langle v(i,j)\rangle + a_{ij}\cos(2\pi f_{ij}t + \varphi_{ij}) + v_f(i,j;t), \quad (17)$$

where $v(i,j;t)$ is the vertical component of the velocity in grid cell (i,j); $\langle v(i,j)\rangle$ is its time-average; a_{ij}, f_{ij}, and φ_{ij} are the amplitude, frequency, and phase to be fitted, respectively; and $v_f(i,j;t)$ is the "turbulent" part in grid cell (i,j). The Reynolds stresses can now be recalculated using v_f:

$$\langle v_f'(i,j)v_f'(i,j)\rangle = \left(\frac{1}{322}\sum_{k=0}^{322} v_f(i,j;k)v_f(i,j;k)\right) - \langle v_f(i,j)\rangle^2. \quad (18)$$

The u-component of the velocity and the other two stresses are treated similarly.

The resultant stresses are shown in Figure 13. The figure shows the profiles for one grid row of $j = 5$. The figure demonstrates that removing the contribution of the vortices has a significant effect on the stresses. It is also seen from the figure that the series may be somewhat short so that the calculation using the time series velocity data, shown as closed symbols in Figure 13, does not completely match the results in Figure 7. With the removal of the vortical structures, relatively flat normal stresses are obtained that have values close to the minimum in $\langle v'v'\rangle$. The turbulence intensities defined in Eq. 15 now drop to around 90%. Notice that the uncorrected shear stress does not follow a Boussinesq approximation, whereas the corrected one does.

It can be concluded from this analysis that the high-frequency content of the normal stresses, that is, the "turbulence," has a rather flat profile with a magnitude of 50–100 cm^2/s^2. This is, however, still an order of magnitude higher than the bubble-induced normal stress, which is only around 5 cm^2/s^2 according to Eqs. 8 and 9. When combined with similar findings for the shear stress in the "Reynolds stresses" subsection, this suggests that in the buoyancy-induced flow of bubble columns, the contribution to the stress due to small-

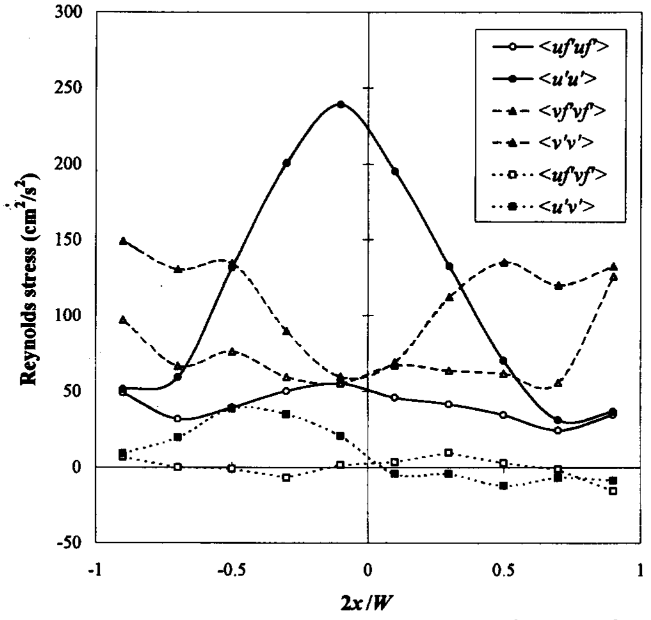

Figure 13. Reynolds stresses for the time series: high-frequency fluctuations (open symbols); total velocity (closed symbols).

scale shear-induced vorticity dominates over the bubble-induced stress.

Results of the 32-cm Case

In the 32-cm column the flow behavior and associated Reynolds stress analysis are more complicated because the vortical structures at low and intermediate gas velocities are not as dominant as in the smaller columns. The flow is investigated at four different gas rates. For the two lowest U_{sup} of 0.4 cm/s and 0.6 cm/s, the flows are in the dispersed regime. For $U_{\mathrm{sup}} = 1.2$ cm/s and 1.9 cm/s, the four-region flow is found, although at the highest gas rate the two bubble streams merge in the middle section of the column.

At $U_{\mathrm{sup}} = 0.4$ cm/s, the profile of the averaged vertical velocity in the lower section clearly marks the position of the injectors. Above the location of the injectors, the liquid rises on average, and in between the liquid flows downward. The overall circulation is established higher in the column, although some influence of the individual bubble streams is still observable, as shown in Figure 14. The corresponding Reynolds stresses for the lower section are given in Figure 15. Even at these low gas rates, the magnitude of the normal stresses is about 30 $\mathrm{cm}^2/\mathrm{s}^2$. This is relatively close to the value of the normal stresses due to the high-frequency turbulence discussed in the previous section, and further demonstrates that the bubble-induced contribution to the normal stresses can be neglected. Note that the shear as well as the normal stresses have their local maxima at the same locations at the maxima of $\langle v \rangle$, that is, directly above the injection points. Similar findings hold for the middle section. Figure 16 demonstrates that at a gas velocity of 0.6 cm/s the overall circulation is observable and that the presence of the gas injectors are still evident in the lower section of the column. The normal stresses are flatter and have a value of 60 $\mathrm{cm}^2/\mathrm{s}^2$. The shear stress in either case shows scattering, and does not indicate a Boussinesq type of behavior with the existing set of data. It should be noted that Figures 14 through 21 (except Figure 19) show only left side of the column; however, when analyzed, their original images are slightly larger, as shown in Table 1, that is, the field of view covers from the left wall to a small portion in the right side of the center of the column.

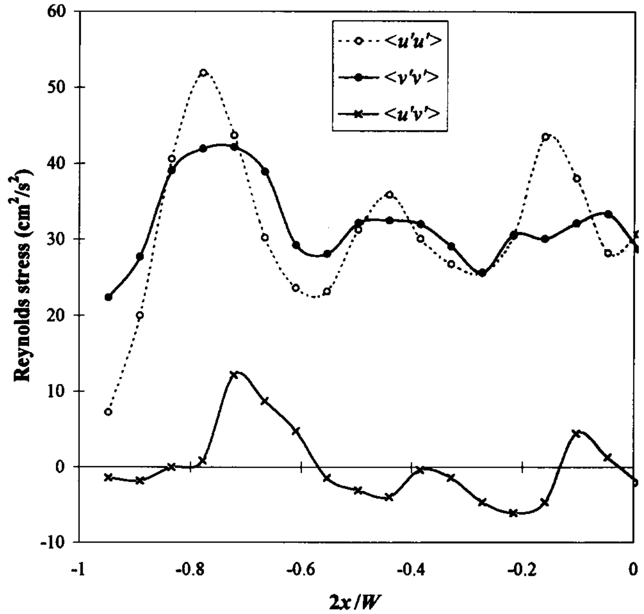

Figure 15. Reynolds stress profiles for the lower section of the left half of the 32-cm column at $U_{\mathrm{sup}} = 0.4$ cm/s.

At $U_{\mathrm{sup}} = 1.2$ cm/s, the four-region flow is observable as seen in Figure 17, with downward flow close to the walls as well as in the center at the upper part of the column. At the

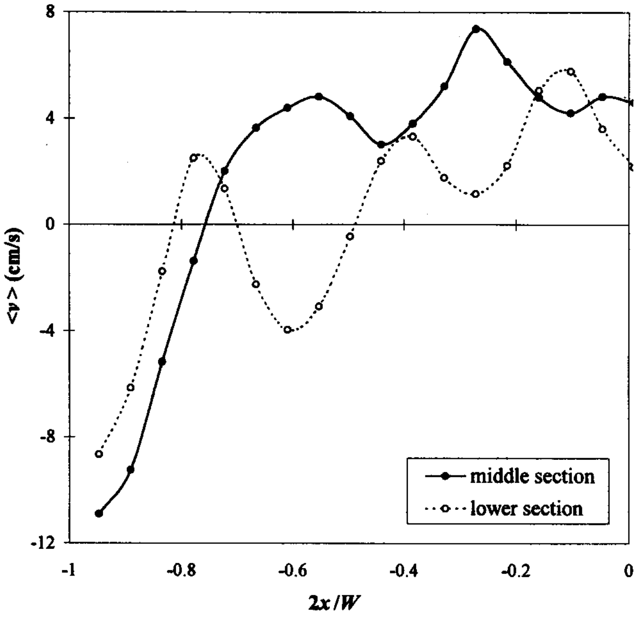

Figure 14. Averaged velocity profiles for the left half of the 32-cm column at $U_{\mathrm{sup}} = 0.4$ cm/s.

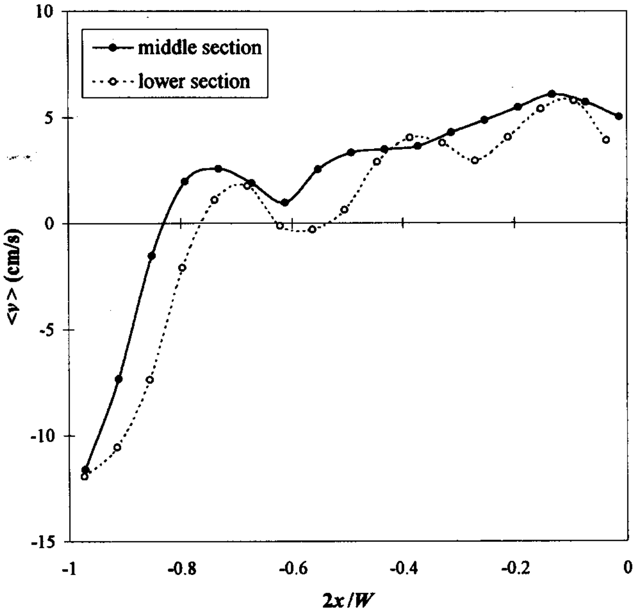

Figure 16. Averaged velocity profiles for the left half of the 32-cm column at $U_{\mathrm{sup}} = 0.6$ cm/s.

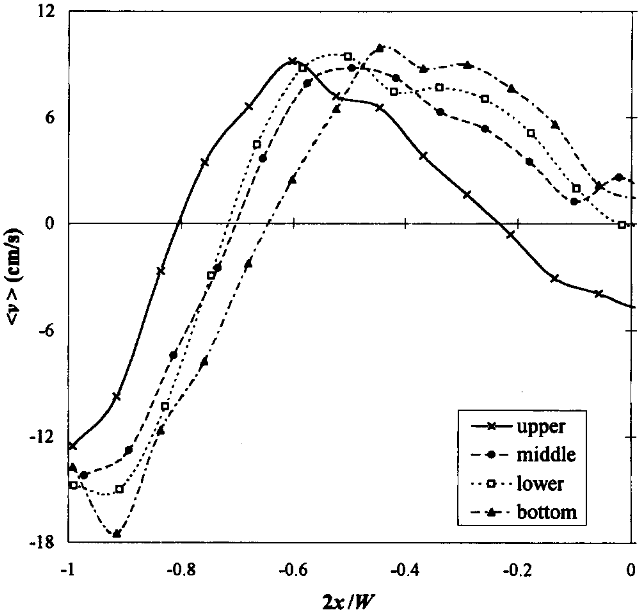

Figure 17. Averaged velocity profiles for the 32-cm column at $U_{sup} = 1.2$ cm/s.

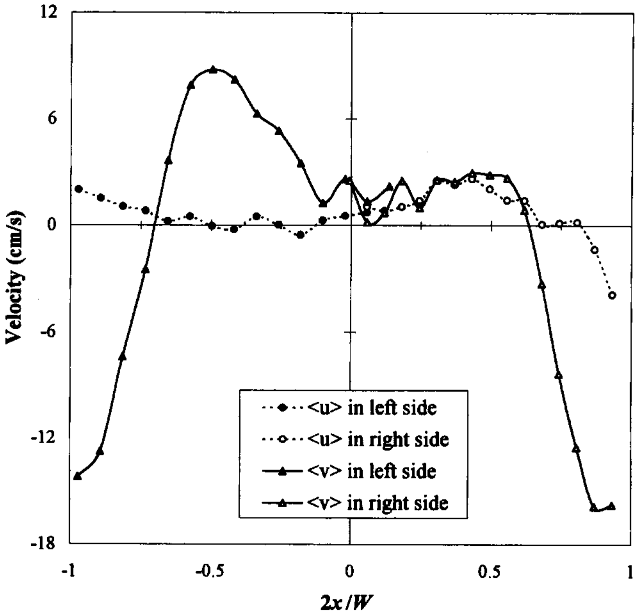

Figure 19. Averaged velocity profiles for the middle section of the 32-cm column at $U_{sup} = 1.2$ cm/s.

lower portions of the column, this minimum in the center shifts from negative to slightly positive. Accordingly the position of the maximum upward average velocity shifts toward the column center, but its magnitude remains about 10 cm/s. In the central plume region, vortical structures are also observed, but the flow is not as regular as in the wall region. Even in the wall region, the vortical structures are less coherent in regards to size and frequency than in the 11-cm and 15-cm cases; furthermore, they no longer span the entire width of the column. The normal stresses, therefore, do not have the pronounced peaks as previously seen for the smaller columns. Instead, the profiles are rather flat, with $\langle u'u' \rangle$ decreasing and $\langle v'v' \rangle$ increasing toward the wall, as seen in Figure 18. In the lower part of the column, $\langle u'u' \rangle$ is somewhat larger than $\langle v'v' \rangle$; and in the upper part, the opposite is true. In the upper section, the normal stress $\langle u'u' \rangle$ has its maximum of 150 cm^2/s^2 at the same position where $\langle v \rangle$ peaks, and $\langle u'u' \rangle$ decreases to 100 cm^2/s^2 toward the center. Although Figure 19 demonstrates that the averaged vertical liquid profile is not symmetric, the stresses are. This may be caused by the absence of the dominating vortices. The turbulence of the "high-frequency background" is more or less constant as discussed in the "Time series" subsection. The magnitude of the normal stresses in the central part of the column are given in Table 5. The shear stress for $U_{sup} = 1.2$ cm/s also does not follow a Boussinesq type of behavior. It should be noted that the shear stress is still rather sensitive to the number of independent vector fields used. Many more fields are presumably necessary for a decisive analysis of the shear.

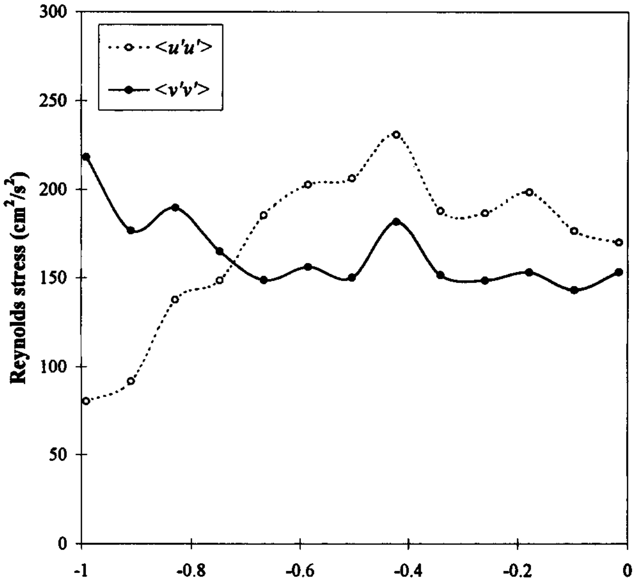

Figure 18. Reynolds-stress profiles for the lower section of the 32-cm column at $U_{sup} = 1.2$ cm/s.

Finally, the results with $U_{sup} = 1.9$ cm/s for the middle section are shown in Figures 20 and 21. The normal stress $\langle u'u' \rangle$ slightly increases toward the center and its maximum is above 400 cm^2/s^2, and $\langle v'v' \rangle$ is relatively flat at a value of about 300 cm^2/s^2. Based on the present results obtained in the 32-cm column, it is seen that the normal stresses rise roughly with the superficial gas velocity to the power 1.5.

Table 5. Magnitude of the Normal Stresses in the 32-cm Column

Section	$\langle u'u' \rangle$ (cm^2/s^2)	$\langle v'v' \rangle$ (cm^2/s^2)
Bottom	150	150
Lower	180	150
Middle	150	170
Upper	130	170

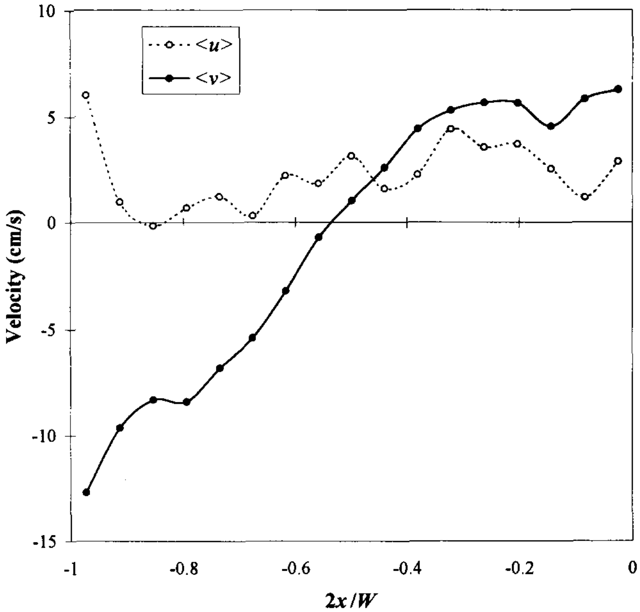

Figure 20. Averaged velocity profiles for the 32-cm column at $U_{\text{sup}} = 1.9$ cm/s.

Concluding Remarks

The flow analysis of bubble columns based on the PIV technique reveals that the flow in the two smaller columns of 11 cm and 15 cm is dominated by the vortical structures. Their contribution causes the Reynolds normal stresses to peak, that is, $\langle u'u' \rangle$ peaks in the center and $\langle v'v' \rangle$ peaks close to the wall. Performing a time-series analysis of the flow field made it possible to separate the contribution of the vortical structures from the high-frequency fluctuations in the normal stresses. Removing the contribution of the vortical structures renders relatively flat normal stress profiles. The turbulence intensities are on the order of 200% when the maximum velocity is used. When the influence of the vortices is removed, the turbulence intensity of the "background" is around 90%. The normal stresses are an order of magnitude larger than the shear stress. The shear stress is seen to follow a Boussinesq behavior. The eddy viscosities are around 5×10^{-4} m^2/s. Reasonable estimates of the eddy viscosities can also be obtained from a k-ϵ model using the measured normal stresses to estimate the turbulent kinetic energy. In all cases investigated, the bubble-induced contribution to the stresses is negligible. The flow in the 32-cm case demonstrates much less order. The vortical structures vary in size and are not as dominant. As a consequence the normal stresses have rather flat profiles and the shear stress does not exhibit a Boussinesq behavior.

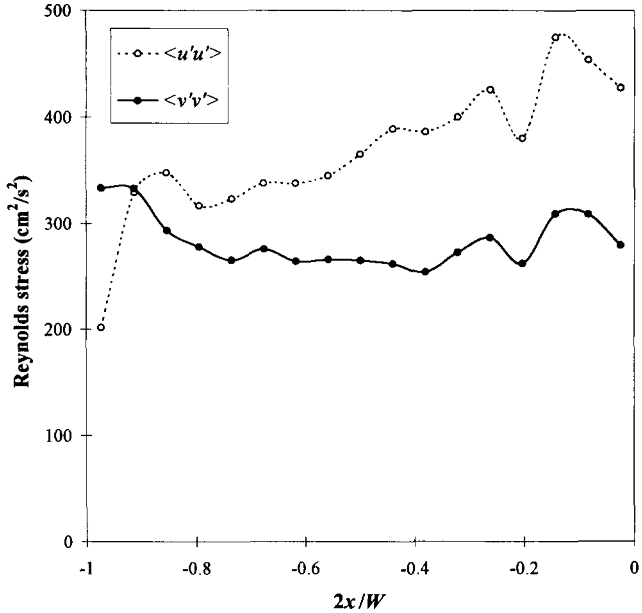

Figure 21. Reynolds-stress profiles for the middle section of the 32-cm column at $U_{\text{sup}} = 1.9$ cm/s.

Acknowledgment

The authors acknowledge the financial support of the National Science Foundation Grant CTS-9528380; and R. F. Mudde especially acknowledges the Nederlandse Organisatie voor Wetenschappelijk Onderzoek (NWO Grant R63-173).

Notation

u' = fluctuating components of the liquid velocity independent of bubbles; fluctuating components of the liquid velocity, defined as $u' = u - \langle u \rangle$
u'' = fluctuating horizontal component of the liquid velocity due to agitation of bubbles
$\langle u''v'' \rangle$ = Reynolds shear stress associated with flucutations in the liquid due to bubble agitation
v_f = "high" frequency part of the velocity in a grid cell after removing the average and contribution of the vortical structures
v_f' = fluctuating part of v_f, defined as $v_f' = v_f - \langle v_f \rangle$
v_l' = fluctuating part of the liquid velocity
ν_t'' = eddy viscosities associated with bubble-agitated fluctuations

Literature Cited

Chen, R. C., and L.-S. Fan, "Particle Image Velocimetry for Characterizing the Flow Structure in Three-Dimensional Gas-Liquid-Solid Fluidized Beds," *Chem. Eng. Sci.*, **47**, 3615 (1992).

Chen, R. C., J. Reese, and L.-S. Fan, "Flow Structure in a Three-Dimensional Bubble Column and Three-Phase Fluidized Bed," *AIChE J.*, **40**, 1093 (1994).

Devanathan, N., D. Moslemian, and M. P. Dudukovic, "Flow Mapping in Bubble Columns Using CARPT," *Chem. Eng. Sci.*, **45**, 2285 (1990).

Devanathan, N., M. P. Dudukovic, A. Lapin, and A. Lübbert, "Chaotic Flow in Bubble Column Reactors," *Chem. Eng. Sci.*, **50**, 2661 (1995).

Elghobashi, S., "On Predicting Particle-Laden Turbulent Flows," *Appl. Sci. Res.*, **52**, 309 (1994).

Franz, K., T. Börner, H. J. Kantorek, and R. Buchholz, "Flow Structures in Bubble Columns," *Ger. Chem. Eng.*, **7**, 365 (1984).

Grevskott, S., B. H. Sannæs, M. P. Dudukovic, K. W. Kjarbo, and H. F. Svendsen, "Liquid Circulation, Bubble Size Distributions, and Solids Movement in Two- and Three-Phase Bubble Columns," *Chem. Eng. Sci.*, **51**, 1703 (1996).

Groen, J. S., R. G. C. Oldeman, R. F. Mudde, and H. E. A. van den Akker, "Coherent Structures and Axial Dispersion in Bubble Column Reactors," *Chem. Eng. Sci.*, **51**, 2511 (1996).

Hills, J. H., "Radial Non-uniformity of Velocity and Voidage in a Bubble Column," *Trans. Inst. Chem. Eng.*, **52**, 1 (1974).

Lance, M., and J. Bataille, "Turbulence in the Liquid Phase of a Uniform Bubble Air-Water Flow," *J. Fluid Mech.*, **222**, 95 (1991).

Lapin, A., and A. Lübbert, "Numerical Simulation of the Dynamics of Two-Phase Gas-Liquid Flows in Bubble Columns," *Chem. Eng. Sci.*, **49**, 3361 (1994).

Lin, T.-J., J. Reese, T. Hong, and L.-S. Fan, "Quantitative Analysis and Computation of Two-Dimensional Bubble Columns," *AIChE J.*, **42**, 301 (1996).

Lopez de Bertodano, M., R. T. Lahey, and O. C. Jones, "Phase Distribution in Bubbly Two-Phase Flow in Vertical Ducts," *Int. J. Multiphase Flow*, **20**, 805 (1994).

Menzel, T., T. in der Weide, O. Staudacher, O. Wein, and U. Onken, "Reynolds Shear Stress for Modeling of Bubble Column Reactors," *Ind. Eng. Chem. Res.*, **29**, 988 (1990).

Nigmatulin, R. I., "Spatial Averaging in the Mechanics of Heterogeneous and Dispersed Systems," *Int. J. Multiphase Flow*, **5**, 353 (1979).

Reese, J., R. C. Chen, J.-W. Tzeng, and L.-S. Fan, "Characterization of the Macroscopic Flow Structure in Gas-Liquid and Gas-Liquid-Solid Fluidization Systems Using Particle Image Velocimetry," *Int. Video J. Eng. Res.*, **3**, 17 (1993).

Reese, J., R. C. Chen, and L.-S. Fan, "Three-Dimensional Particle Image Velocimetry for Use in Three-Phase Fluidization Systems," *Exp. Fluids*, **19**, 367 (1995).

Sato, Y., M. Sadatomi, and K. Sekoguchi, "Momentum and Heat Transfer in Two-Phase Bubbly Flow—I," *Int. J. Multiphase Flow*, **7**, 167 (1981).

Tzeng, J.-W., R. C. Chen, and L.-S. Fan, "Visualization of Flow Characteristics in a 2-D Bubble Column and Three-Phase Fluidized Bed," *AIChE J.*, **39**, 733 (1993).

Yang, Y. B., N. Devanathan, and M. P. Dudukovic, "Liquid Backmixing in Bubble Columns via Computer-Automated Radioactive Particle Tracking (CARPT)," *Exp. Fluids*, **16**, 1 (1993).

Manuscript received July 5, 1996, and revision received Dec. 5, 1996.